Thermal Science and Engineering Progress 44 (2023) 102065

Contents lists available at ScienceDirect

Thermal Science and Engineering Progress

journal homepage: www.sciencedirect.com/journal/thermal-science-and-engineering-progress

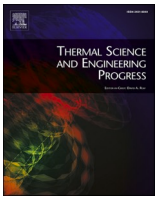

Arrangement optimization of spherical dimples inside tubes based on machine learning for realizing the optimal flow pattern

Chunyu Shi, Yuhao Zhu, Minjie Yu, Zhichun Liu *

School of Energy and Power Engineering, Huazhong University of Science and Technology, Wuhan 430074, China

ARTICLE INFO

Keywords:
Convective heat transfer
Dimple
Machine learning
Optimization
Numerical simulation

ABSTRACT

Optimizing the arrangement of dimples in a dimpled tube can alter the flow field structure and improve its heat transfer performance. However, direct optimization through numerical simulation techniques is challenging due to the high nonlinearity and time-consuming nature of the heat transfer process. This study proposes a novel optimization method based on a surrogate model combined with machine learning technology. By considering the relative positions of the dimples as design variables and the comprehensive performance of the dimpled tube as the optimization objective, the optimal arrangement of dimples is achieved, and the flow field structure under the optimal layout configuration is determined. The results indicate that the optimal design involves five dimples forming a V-shaped dimpled strip, which deflects the flow and disrupts the boundary layer development. The optimal flow pattern with multi-longitudinal vortexes is formed which promotes the mixing between the cold and hot fluids and intensifies heat transfer with a moderate pressure loss. The performance of the optimal structure is evaluated within a Reynolds number range of 600 to 1200. As a result, the heat transfer capacity is increased by 5.376–8.819 times compared to plain tubes, with an increase in the flow resistance factor by 3.102–5.264. The comprehensive performance achieves a range of 3.683–5.069. Furthermore, the research conducted particle image velocimetry experiments to observe the flow field structure inside the optimized tube, thus validating the effectiveness of the optimization. The study holds significant importance in guiding the design of heat exchangers, improving the economic efficiency of energy utilization.

Introduction

Currently, fossil fuels continue to dominate the structure of energy consumption, which will not only deplete natural resources but also adversely impact the local climate [1]. Enhancing energy utilization efficiency can alleviate the energy shortage crisis and is crucial for accelerating the transition to clean energy, playing a significant role in achieving global sustainable development goals. Heat exchanger tubes, as a fundamental heat transfer unit, find extensive application in traditional industries such as thermal power generation, chemical processing, and mechanical power equipment, which are also utilized in clean energy equipment, including parabolic trough solar receiver, solar tower receivers, and nuclear power plants. By enhancing heat transfer technology to improve the performance of heat exchanger tubes enables the reduction of irreversible losses in the energy transfer process, making it a crucial pathway for enhancing energy utilization efficiency.

Heat transfer enhancement technologies can be classified into active and passive methods. Passive methods, which offer advantages such as easier maintenance and independence from external power supply, are more popular. These methods employ special structures, such as tube inserts [2] or artificial wall roughness [3], to enhance performance. Dimples are enhanced heat transfer structures mounted on the wall which enables a more considerable thermal performance with the flow resistance slightly increased by promoting the mixing of high and low-temperature fluids [4]. Numerous investigations and modifications have been proposed for dimpled tubes, with some focusing on the structural parameters of the dimple. Vicente et al. [5] conducted isothermal pressure drop experiments to investigate the effects of dimple height on hydraulic behavior in tubes. They showed that, the modification of dimple height accelerates the flow transition from laminar to turbulent and reduces the critical Reynolds number (*Re*) to 1400. Kumar et al. [6] altered the span-wise and stream-wise spacings of the dimples to experimentally investigate the variation of thermal–hydraulic behavior. The enhancement of 3.43 times in thermal performance was finally achieved. They found that as the depth of the dimples increases, the heat transfer enhancement becomes more pronounced. This is attributed to the intensified vortex and accompanying secondary flow

* Corresponding author.
E-mail address: zcliu@hust.edu.cn (Z. Liu).

https://doi.org/10.1016/j.tsep.2023.102065
Received 15 March 2023; Received in revised form 26 May 2023; Accepted 14 August 2023
Available online 16 August 2023

Nomenclature

d_p	dimple pitch (mm)
f	friction factor
H	dimple depth (mm)
h	heat transfer coefficient ($W{\cdot}m^{-2}{\cdot}K^{-1}$)
I	turbulent intensity
L	tube length (mm)
L_d	length of design unit (mm)
N_m	number of surrogate updating
Nu	Nusselt number
Pr	Prandtl number
q	heat flux density ($W{\cdot}m^{-2}$)
r_0	tube radius (mm)
Re	Reynolds number
T_{in}	inlet temperature of fluid (K)
U_{in}	inlet velocity of fluid ($m{\cdot}s^{-1}$)

Greek symbols

α	synergy angle (°)
θ	circumferential angle (°)
λ	thermal conductivity ($W{\cdot}m^{-1}{\cdot}K^{-1}$)
μ	fluid dynamic viscosity ($kg{\bullet}m^{-1}{\bullet}s^{-1}$)
ρ	material density ($kg{\cdot}m^{-3}$)
φ_p	dimple diameter (mm)
ω	staggered angle of dimples in stream wise direction (°)

Subscripts

ave	average value
f	fluid phase
local	local value
max	maximum value
min	minimum value
pla	plain tube
pred	predicted value
test	test section
theo	theoretical value

discharged from the dimples. Saini and Verma [7] developed the correlations for the Nusselt number and friction factor using relative roughness height and relative pitch as parameters, which were derived from experimental data collected for solar air heaters with dimple-shaped artificial roughness.

Other studies have been conducted on the shape of the dimples. Li et al. [8] and Sabir et al. [9] conducted numerical simulations to compare three different geometrical dimples, namely cone, sphere, and ellipsoid. The spherical dimples exhibited the highest thermal–hydraulic performance at *Re* less than 4000, whereas the ellipsoidal dimples demonstrated better performance at *Re* greater than 4000. Xie et al. [10] proposed a teardrop-shaped dimple and they found that the area for poor heat transfer is reduced distinctively, and the overall heat transfer rate obtains an apparent improvement. Zhang et al. [11] revealed the flow and heat characteristics in rectangular channels combined with convex-dimples and grooves. They concluded that the placement of dimple upstream of the groove helps to generate the rotating flow which leads to an upstream movement of flow reattachment. Xie et al. [12], Liu et al. [13], and Waghmare et al. [14] employed mechanical extruded method to develop dimpled tubes, which have a smooth transition in the wall edge of the cavity. The researchers indicated that the proposed structure exhibits superior overall thermal performance due to the tube's ability to provide larger and more uniformly distributed turbulent kinetic energy. Dagdevir et al. [15] performed a numerical simulation on an enhanced tube with the trapezoidal dimples, and the effects of dimple diameter, trapezoid angle, and pitch length were involved. Finally, they obtained a relatively optimal structure with comprehensive performance as 1.7194. Zhang et al. [16] investigated the thermal performance for an enhanced tube with cross-combined ellipsoidal dimples. They showed that the proposed structure brings an obvious improvement of temperature gradient in the core domain of the tube. Ahmad et al. [17] proposed a double-dimpled corrugated pipe and evaluated the thermo-hydrodynamic performance with varying *Re* and nanoparticle volume concentrations. They found that optimizing the shape of corrugated pipes, particularly those with a more complex geometrical configuration, improves their heat transfer efficiency. At $Re = 20{,}000$ for the base fluid, the heat transfer efficiency in the dimpled pipe was calculated to be 31.16% higher than that in the smooth pipe.

The literature mentioned above focuses on optimizing the structural parameters and shapes of dimples. However, these approaches have limited performance enhancement for dimpled tubes because they have minimal impact on altering the flow field structure and primarily disrupt fluid flow to achieve enhancement. Optimizing the arrangement of the dimples can deflect the flow and promote the formation of a low resistance flow field structure within the tube, thereby resulting in more significant performance improvements. A general consensus on the optimal flow pattern has been developed by combining the calculus of variations with the field synergy principle [18], entropy generation minimization principle [19], and exergy minimization principle [20]. The studies all indicate that the optimal flow pattern is the multi-longitudinal swirl flow, which is then constructed by inserting deflectors [21]. There has been limited research conducted on constructing the optimal flow pattern by adjusting the arrangement of dimples. When constructing optimal fields through structural design, most scholars rely on a combination of experience and experimentation to obtain the best result by comparing multiple sets of experiments. Due to the inherent limitations of empirical knowledge, there are still numerous opportunities for optimization in the final design. Therefore, it is significant to utilize optimization algorithms to explore the optimal arrangement of dimples for verifying the optimal flow pattern and enhancing the performance of the dimpled tube.

With the advancements in global optimization algorithms, numerous intelligent algorithms inspired by natural principles, such as the genetic algorithm (GA), particle swarm optimization (PSO), and simulated annealing algorithm (SA), have emerged. These optimization algorithms have greatly facilitated the optimization of heat transfer devices. However, their effective application relies on the availability of accurate mathematical models that describe the relationship between design variables and performance. Due to the increasing complexity of heat transfer optimization problems and the limited computational resources, the development of suitable mathematical models for performance prediction has become a critical limitation in the application of optimization algorithms. A surrogate model is a mathematical expression that approximates the relationship between input and output variables. By utilizing these surrogate models, the computationally expensive process of conducting computational fluid dynamics (CFD) calculations can be replaced with inexpensive mathematical calculations. This enables the optimization of heat transfer elements under more feasible conditions. Common surrogate models used in optimization include response surface models (RSM), artificial neural network models (ANN) [22], radial basis neural network models (RBN) [23], Kriging model (KRG) [24], and support vector regression models (SVR) [25]. Samad et al. [26,27] performed a multi-objective optimization of the dimpled channel by using the geometric variables of the dimples as design variables and considering the *Nu* number and friction factor as objective functions. The study employed a novel surrogate model for

optimization, which is essentially a weighted average of the basic surrogates, RSM, KRG, and RBN. The results demonstrated that the optimized shape exhibited a 70.8% increase in thermal performance compared to the reference geometry. Kim et al. [28] utilized the KRG approach to optimize a cooling channel featuring staggered elliptic dimples. The study achieved two extreme optimum designs on the pareto optimal front, focusing on heat transfer and pressure loss. These designs resulted in a 32.8% increase in heat transfer rate and a 34.6% decrease in pressure loss, respectively, compared to the reference design. Lei et al. [29] conducted an optimization study on dimpled tubes using RSM. The chosen design parameters included the dimple diameter, depth-to-diameter ratio, spacing-to-diameter ratio between adjacent dimples, and the number of dimples in the transverse cross-section of the tubes. Additionally, the comprehensive performance of 1.23 was obtained after optimization.

Traditional surrogate models offer the advantage of high optimization efficiency. However, these models encounter limitations when addressing heat transfer optimization problems characterized by high nonlinearity. These limitations restrict their wider application in the field of heat transfer optimization. Firstly, traditional surrogate models primarily focus on achieving global accuracy during data fitting. While this approach guarantees a certain range of prediction errors across the entire dataset, it may lead to distortions in local features. Consequently, this can lead to inconsistencies between the actual and predicted values of the optimization results. Secondly, in constructing a traditional surrogate model, there is no standardized criterion for determining the optimal sample size. Instead, it is necessary to perform continuous testing to ascertain the suitable sample size that fulfills the accuracy requirements. This undoubtedly adds to the complexity of surrogate model construction.

Based on the above, this paper focuses on investigating the impact of dimple arrangement on performance and conducts optimization research on dimpled tubes to optimize the flow field structure and significantly enhance the overall performance within the tubes. To ensure the reliability of optimization results and the efficiency of the optimization process, this study combines machine learning with intelligent optimization algorithms to develop a novel heat transfer optimization method based on a dynamic surrogate model. Through a comparison with traditional surrogate models, the advantages of this optimization method in optimizing the arrangement of the dimples have been evaluated. By analyzing and comparing the velocity and temperature distribution before and after optimization, the mechanisms behind the performance improvement are elucidated. Furthermore, a particle image velocimetry platform is constructed to observe the actual flow field structure within the tube, thus verifying the reliability of the simulation method and ensuring the effectiveness of the optimization. This work offers novel insights to guide the structural design for enhancing heat transfer. The method developed in this paper provides engineers with a means to reduce unnecessary time-consuming tasks and improve optimization efficiency.

Computational model and numerical method

Physical description of the problem

In this paper, the heat transfer and flow characteristics in enhanced tubes with spherical dimples are numerically investigated. The initial arrangement of the dimples is shown in Fig. 1. A total of 360 dimples with the diameter (φ_p) and depth (H) are equidistantly distributed throughout the entire test section. Six dimples are uniformly arranged in the circumferential direction. The adjacent dimples in the streamwise direction are arranged with a pitch (d_p) and staggered angle (ω). The computational domain consists of three sections, where the entrance and exit sections adopt plain tubes with a radius (r_0) to eliminate negative effects. The lengths of the three sections are selected as 100 mm, 900 mm, and 250 mm, respectively. The geometric dimensions of the numerical model are listed in Table 1.

Considering that a large number of design parameters will consume extensive computing resources during the optimization process, the section shown in Fig. 2 (a) with a circumferential angle OBB' = 120° and a length of L_d = 30 mm is selected as the design unit. The selection is based on the periodic arrangement in both the circumferential and axial directions. Dimples within the design unit are symmetrically arranged and are divided into three groups based on their location. Those located at the symmetry planes of $\theta = 0, 120°$, and $-120°$ are named *Di*. Dimples situated at the unit interfaces of $\theta = 60°$, 180°, and $-60°$ are named *Dc*. Additionally, those located between the symmetry plane and the interface plane in the circumferential direction are named *Df*. Four parameters, namely d_1, d_2, d_3, and β, have been derived in this study. These parameters represent the distances from the center of *Di*, *Dc*, *Df* to the start plane for the design unit, as well as the angle from the center of *Df* to the symmetry plane, as shown in Fig. 2 (b) and (c). The coordinates of all dimples can be obtained by employing a cylindrical coordinate system, as shown in Table 2. Additionally, Table 3 provides the values for the original staggered arrangement.

Governing equations and boundary conditions

In this study, the flow is assumed to be fully developed, laminar, and Newtonian, while ignoring heat generation by viscous dissipation. Considering the small temperature variation range, the physical properties can be regarded as constant with temperature. The effects of

Table 1
The geometric dimensions of the numerical model.

Dimensions	Value	Unit
Total length, $L_1 + L_2 + L_3$	1250	mm
Tube radius, r_0	20	mm
dimple diameter, φ_p	8	mm
dimple depth, H	2	mm
adjacent dimples pitch, d_p	15	mm
staggered angle, ω	30	°

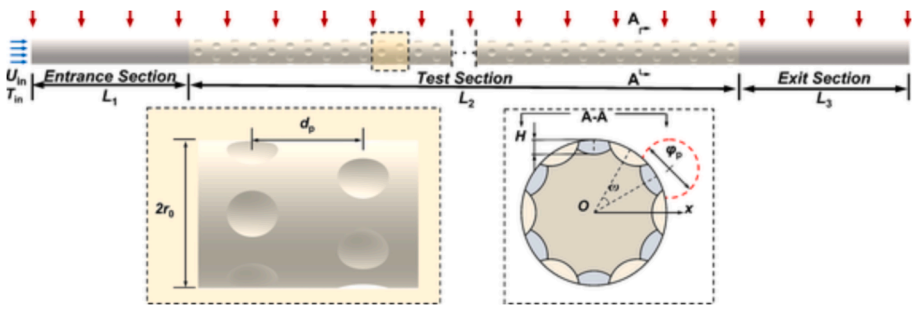

Fig. 1. Computational domain with initial dimpled arrangement.

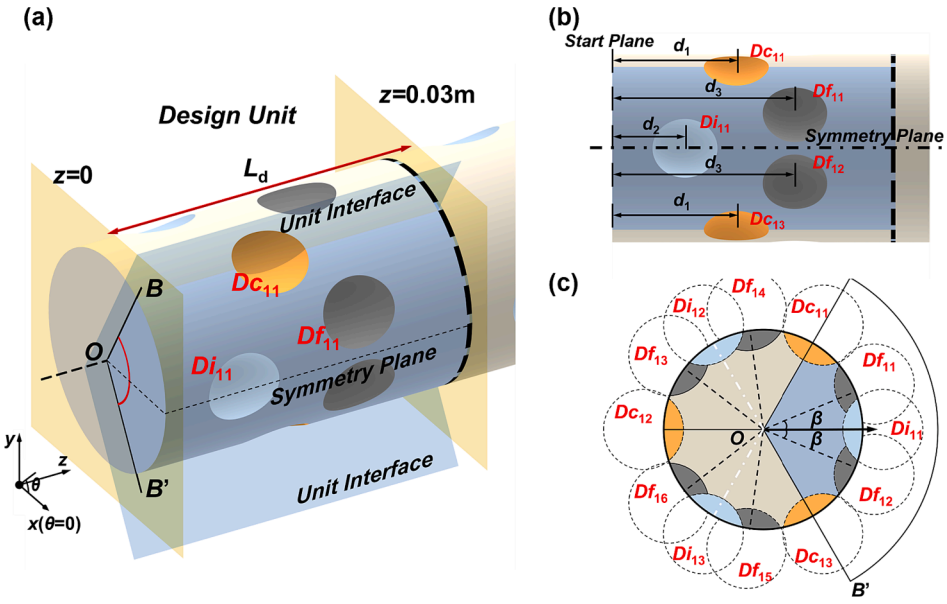

Fig. 2. Design unit and parameters for arrangement of dimples (a) schematic of design unit (b) parameters for dimpled arrangement (c) parameters in cross section.

Table 2
The cylindrical coordinates for all dimples in test section.

No.	Cylindrical coordinates (r, θ, z) (a = 1, 2, …, n)	*No.*	Cylindrical coordinates (r, θ, z) (a = 1, 2, …, n)
Di_{a1}	(r_0, 0, d_2+(a-1) × L_d)	Df_{a1}	(r_0, β, d_3+(a-1) × L_d)
Di_{a2}	(r_0, 120°, d_2+(a-1) × L_d)	Df_{a2}	(r_0, -β, d_3+(a-1) × L_d)
Di_{a3}	(r_0, −120°, d_2+(a-1) × L_d)	Df_{a3}	(r_0, 120°+β, d_3+(a-1) × L_d)
Dc_{a1}	(r_0, 60°, d_1+(a-1) × L_d)	Df_{a4}	(r_0, 120°-β, d_3+(a-1) × L_d)
Dc_{a2}	(r_0, 180°, d_1+(a-1) × L_d)	Df_{a5}	(r_0, −120°+β, d_3+(a-1) × L_d)
Dc_{a3}	(r_0, −60°, d_1+(a-1) × L_d)	Df_{a6}	(r_0, −120°-β, d_3+(a-1) × L_d)

Table 3
Values of the original staggered arrangement for enhanced tube.

Parameters	Value
d_1	7.5 mm
d_2	7.5 mm
d_3	22.5 mm
β	30°

gravity and radiation heat transfer are negligible. Water is selected as the working fluid, and its properties are assumed to be constant as provided in Table 4. The governing equations for this study encompass continuity, Navier-Stokes, and energy equations, denoted as Eqs. (1)-(3) in tensor form.

$$\frac{\partial u_i}{\partial x_i} = 0 \tag{1}$$

$$\rho u_i \frac{\partial u_j}{\partial x_i} = -\frac{\partial p}{\partial x_i} + \frac{\partial}{\partial x_i}\left(\mu \frac{\partial u_j}{\partial x_i}\right) \tag{2}$$

$$\rho c_p \left(u_i \frac{\partial T}{\partial x_i}\right) = k\left(\frac{\partial^2 T}{\partial x_i^2}\right) \tag{3}$$

Table 4
The properties of working fluids.

Properties	ρ (kg·m^{-3})	c_p (J·kg^{-1}·K^{-1})	λ (W·m^{-1}·K^{-1})	μ (kg·m^{-1}·s^{-1})
Value	998.2	4182	0.6028	0.0010074

The entrance boundary is considered to be fully developed before the fluid flows into the model, and the corresponding velocity and temperature distributions are satisfied by: $u(r) = 2u_{in}\left[1 - \left(\frac{r}{r_0}\right)^2\right]$ (4)

$$T(r) = T_{in} + \frac{qr_0}{\lambda_f} + \left[\left(\frac{r}{r_0}\right)^2 - \frac{1}{4}\left(\frac{r}{r_0}\right)^4\right] \tag{5}$$

The Reynolds numbers of this study are in the range of 800 to 1200. Accordingly, the average inlet velocity is calculated as $u_{in} = 0.03 \sim 0.06$ m/s, and the central temperature of the inlet is $T_{in} = 300$ K. The pressure gauge of the outlet is set as $P_{out} = 0$. Wall boundary is considered as no-slip boundary condition with the input heat flux of $q = 2000$ W/(m^2·K).

In this study, the computational domain is discretized using the finite volume method, which transforms Eqs. (1)-(3) into a system of algebraic equations for each node. The second upwind scheme is employed to solve the intermediate point values of the algebraic equations after the discretization process. The pressure–velocity coupling field is solved by the coupled algorithm. The simulations in the present work are completed by commercial software, ANSYS Fluent. The solution process is terminated and considered to be converged when the relative residuals are less than 10^{-5} for the continuity equation and 10^{-7} for the other equations [30].

Data reduction

The velocity and temperature fields can be obtained by numerical analysis. The friction factor (f) is employed to characterize the hydraulic performance which can be calculated from:

$$f = \frac{\Delta p_{test}}{L_2} \frac{2r_0}{(1/2)\rho_f u_{in}^2} \tag{6}$$

The corresponding Reynolds numbers is

$$Re = \frac{2\rho_f U_{in} r_0}{\mu_f} \tag{7}$$

The Nusselt number (Nu) are chosen to evaluate the thermal performance, which can be calculated as

$$Nu = \frac{2hr_0}{\lambda_f} \tag{8}$$

where h is the heat transfer coefficient, which can be calculated as:

$$h = \frac{q_{test}}{\Delta T_{test}} \tag{9}$$

$$\Delta T_{test} = \frac{\left(T_w - T_{test,in}\right) - \left(T_w - T_{test,out}\right)}{\ln\left(\frac{T_w - T_{test,in}}{T_w - T_{test,out}}\right)} \tag{10}$$

$$T_{test,in} = \left.\frac{\int_0^{r_0} u_{r,z} T_{r,z} r dr}{\int_0^{r_0} u_{r,z} r dr}\right|_{z=0.} \tag{11}$$

$$T_{test,out} = \left.\frac{\int_0^{r_0} u_{r,z} T_{r,z} r dr}{\int_0^{r_0} u_{r,z} r dr}\right|_{z=0.15m} \tag{12}$$

Performance evaluation criterion (*PEC*) is employed to evaluate the comprehensive performance of the heat transfer and flow resistance:

$$PEC = \frac{Nu/Nu_{\mathrm{pla}}}{\left(f/f_{\mathrm{pla}}\right)^{1/3}} \tag{13}$$

Grid independence and model validation

Due to the irregular structure of the dimples, the structured grid cannot adequately characterize its specific features. Therefore, an unstructured mesh is used to partition the computational domain. This paper employs polyhedral grids to discretize the computational domain, which involves a combination of tetrahedral and hexahedral meshing methods to generate polyhedral elements that accurately represent complex geometries, as shown in Fig. 3. An eight-layer boundary layer grid is generated near the inner wall to accurately capture the large variations in physical quantities. Grid independence verification is performed to assess the impact of the grid number on simulation results. Due to the potential overlap and superposition of dimples as the design parameters change, the complexity of the corresponding models varies, requiring different numbers of meshes to achieve accurate solutions. To ensure complete elimination of the grid's influence, grid independence is verified using five arrangements with random design parameters. The schematic diagram of the five arrangements and grid division is also shown in Fig. 3. The calculated results at $Re = 1000$ are shown in Table 5. When the number of meshes exceeds 7500000, the relative changes of both *Nu* and *f* are less than 1%, which indicates that the effect of grids number on simulation results is already negligible. Therefore, to save computational time, a grid number of 7,500,000 is selected for the simulations in this study.

Moreover, to ensure the reliability of the calculation results, single-phase flow simulations are conducted separately in both smooth and dimpled tubes using the aforementioned governing equations. For a constant input heat flux, the *Nu* number and *f* for a smooth tube in the laminar flow regime (*Re* less than 2300) can be obtained from the corresponding theoretical equations: $Nu_{\mathrm{pla}} = 4.36$ and $f_{\mathrm{pla}} = 64/Re$. The comparison results under identical operating conditions are shown in Fig. 4 (a). Furthermore, a validation is conducted to assess the numerical accuracy using a discrete double-inclined rib design, similar in structure to the dimples, which also enhances convective heat transfer through artificial roughness on the inner wall. The experimental results of Meng et al. [18] are employed for comparison. As shown in Fig. 4 (b), the numerical solutions are consistent with the experimental results which prove that the numerical method used in this document is precise and effective.

Table 5
Grid independence test.

Case	Grid system	Cells number	*Nu*	Relative error-*Nu*	*f*	Relative error-*f*
Case #1	1	2,391,567	25.726	–	0.628	–
	2	4,711,059	26.373	2.51%	0.651	3.67%
	3	7,745,118	26.675	1.15%	0.658	1.11%
	4	12,163,370	26.802	0.47%	0.663	0.69%
	5	15,494,171	26.840	0.14%	0.665	0.24%
Case #2	1	2,368,109	11.226	–	0.285	–
	2	4,517,933	11.506	2.50%	0.298	4.82%
	3	7,860,585	11.685	1.56%	0.308	3.14%
	4	12,456,707	11.739	0.46%	0.309	0.35%
	5	15,574,168	11.751	0.10%	0.310	0.26%
Case #3	1	2,268,416	18.246	–	0.503	–
	2	4,501,841	19.288	5.71%	0.524	4.27%
	3	7,542,649	19.748	2.39%	0.537	2.40%
	4	12,062,176	19.892	0.73%	0.540	0.60%
	5	15,219,530	19.916	0.12%	0.541	0.22%
Case #4	1	2,249,158	10.423	–	0.318	–
	2	4,618,305	11.059	6.10%	0.326	2.63%
	3	7,762,274	11.279	1.99%	0.330	1.24%
	4	12,175,823	11.345	0.59%	0.333	0.67%
	5	15,375,228	11.375	0.26%	0.333	0.22%
Case #5	1	2,162,539	11.220	–	0.299	–
	2	4,824,690	12.020	7.14%	0.302	1.10%
	3	7,543,071	12.451	3.58%	0.304	0.68%
	4	12,230,251	12.557	0.85%	0.306	0.52%
	5	15,660,687	12.602	0.36%	0.306	0.26%
Case #6	1	2,166,812	17.491	–	0.366	–
	2	4,777,098	18.839	7.71%	0.388	5.91%
	3	7,815,999	19.336	2.64%	0.393	1.45%
	4	12,229,599	19.487	0.78%	0.395	0.59%
	5	15,474,460	19.571	0.44%	0.396	0.25%

Optimization problem and methods

The optimization problem description

Keeping the radius and depth of the dimples constant, a single-

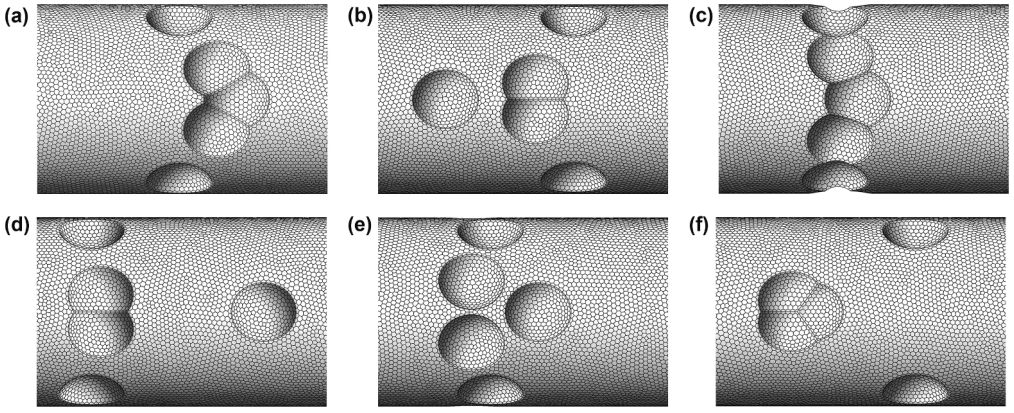

Fig. 3. Mesh generation for dimpled tube.

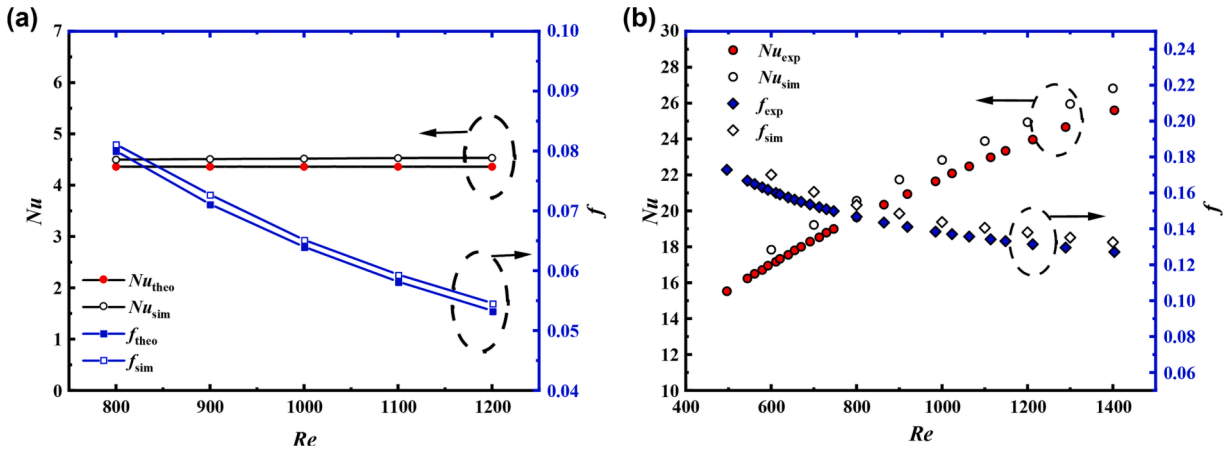

Fig. 4. Obtained numerical results validated with empirical formulas and experiment data (a) numerical simulation verification of smooth tube (b) numerical simulation and experimental verification [18] of the enhanced tube.

objective optimization is conducted to determine the optimal arrangement of the dimples using the design parameters d_1, d_2, d_3, and β. In cases where β exceeds 30°, an identical design to that with β less than 30° can be achieved by interchanging the values of d_1 and d_2. To minimize the likelihood of design duplication, the range of β is restricted to [0, 30°]. Additionally, the distance parameters d_1, d_2, and d_3 are constrained to vary within the range of [5,25] mm, which is imposed due to the limitations of the unit length.

The optimization of forced convection involves the careful consideration of both heat transfer enhancement and resistance increase. To strike a balance between these factors, *PEC* is chosen as the objective for optimization. The goal is to achieve an optimal arrangement of the dimples that minimizes pump power loss while maximizing heat transfer enhancement. Furthermore, to account for performance within the range of *Re* from 600 to 1200, a compromise solution is adopted in this study by selecting $Re = 1000$ as the optimized working condition.

Dynamic surrogate model based on machine learning

In the optimization process, evaluating numerous designs using CFD can be time-consuming. To address this issue, a common approach is to employ surrogate models that approximate CFD calculations. Surrogate models are particularly well-suited for optimizing complex problems due to their rapid computational speed. However, traditional surrogates require a considerable number of sampling points to capture the local features of the actual distribution, which can reduce optimization efficiency. In some cases, achieving accuracy across the entire design space may not be necessary, and it is sufficient to ensure that the surrogate model maintains high accuracy near the optimal value.

Surrogate models based on machine learning (SML) follow a two-step process: initially, a surrogate is constructed using a small set of sample points, and then the model is iteratively updated through machine learning until no further updates are necessary. The use of SML reduces the number of required simulations by excluding redundant points, thereby enhancing efficiency. Additionally, continuous updates of the surrogate model help identify missed local features, resulting in improved accuracy of the optimization results.

Fig. 5 illustrates the key steps involved in constructing an SML framework. The framework consists of two main components. The first component is a surrogate model that characterizes the relationship between the objectives and design parameters. In this study, the Kriging model (KRG) is selected as the surrogate model, which treats the objective function as a Gaussian process and provides a predicted function $\hat{y}(\mathbf{x})$ and variance function $s(\mathbf{x})$ [31]. The second component is an acquisition function, which determines the next point to evaluate based on the distribution of objectives and uncertainties. In this study,

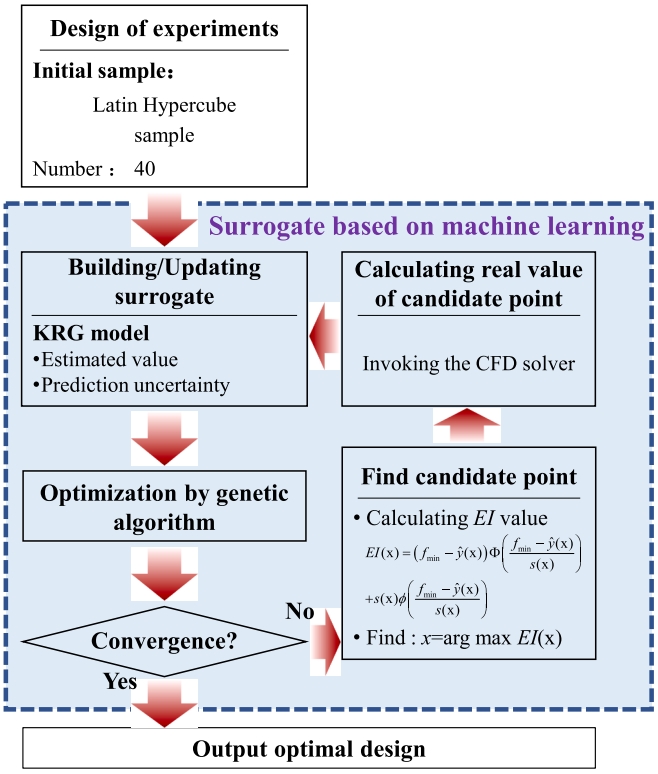

Fig. 5. Framework of constructing surrogate based on machine learning.

the expected improvement (*EI*) function is utilized as the acquisition function, which takes an unknown point × as a random variable following a normal distribution with a mean $\hat{y}(\mathbf{x})$ and standard deviation $s(\mathbf{x})$:

$$Y(\mathrm{x}) \sim N(\hat{y}(\mathrm{x}), s(\mathrm{x})) \tag{14}$$

The improvement of the precise value of an unknown point × to the current optimal solution can also be viewed as a random variable if the current prediction's minimal value is $f_{\min}$:

$$I(\mathrm{x}) = \max[f_{\min} - \hat{y}(\mathrm{x}), 0] \tag{15}$$

The physical meaning of the *EI* function is the expectation of this improved value.

$$EI(\mathrm{x}) = \int_{-\infty}^{f_{\min}} (f_{\min} - \hat{y}(\mathrm{x})) \frac{1}{\sqrt{2\pi}s(\mathrm{x})} \exp\left(-\frac{\hat{y}(\mathrm{x})^2}{2s(\mathrm{x})^2} \right) \mathrm{d}Y \tag{16}$$

Solving this equation yields an expression for the *EI* function as:

$$EI(\mathbf{x}) = (f_{\min} - \hat{y}(\mathrm{x}))\Phi\left(\frac{f_{\min} - \hat{y}(\mathrm{x})}{s(\mathrm{x})}\right) + s(\mathrm{x})\phi\left(\frac{f_{\min} - \hat{y}(\mathrm{x})}{s(\mathrm{x})}\right) \tag{17}$$

Where $\Phi(\cdot)$ and $\phi(\cdot)$ represent for the standard normal distribution's probability density function and cumulative distribution function, respectively. The *EI* value gets larger with a smaller $\hat{y}(x)$ and a larger $s(x)$, which means the optimization process converge towards the minimum prediction value as well as the maximum variance.

In the process of constructing SML, a total of 40 samples are collected to obtain the initial rough model. Subsequently, the *EI* values are calculated using Eqs. (16) and (17) and the candidate point corresponding to the maximum *EI* value is determined. By incorporating the exact value for the candidate point, the model is updating until the convergence conditions are satisfied, i.e., the maximum *EI* value is within 10^{-4}, and the optimal value remained constant in the final 20 updates before termination.

Genetic algorithm

The optimization process is needed to find the optimal solution under the current surrogate model and calculate the location of the maximum *EI* value to find the location of the additional sample points.

Genetic algorithm is a global optimization algorithm developed by learning from the biological evolution mechanism of "survival of the fittest" in nature. In the optimization process, the input parameters are encoded into a fixed-length string as chromosomes, and each digit in the string is considered as the genetic information carried by the chromosomes themselves, and the highly adaptive chromosomes are retained and evolved until the optimal solution is found through continuous crossover, mutation, and selection operations [32]. Table 6 displays the parameters of genetic algorithm.

Results and discussion

Optimization process and validated

The variations of the $PEC_{\max}$ and $EI_{\max}$ with the number of surrogate updates N_m are given in Fig. 6 (a) and (b). The $PEC_{\max}$ changes frequently at the beginning of the model updating, but when $N_m = 75$, the $PEC_{\max}$ increases to 4.904 and no longer changes until the optimization is terminated as the $EI_{\max}$ decreases to below 10^{-4} at $N_m = 126$. Combined with the variation trend of the $EI_{\max}$ shown in Fig. 6 (b), the $EI_{\max}$ undergoes more significant changes in the early stage, indicating a tendency to converge to a local optimum due to the limited number of sample points. Each abrupt increase in the $EI_{\max}$ indicates that the optimization process jumps out of the local optimum and the $PEC_{\max}$ changes accordingly. As the optimization proceeds, the $EI_{\max}$ gradually stabilizes and decreases, indicating that the current model has a high prediction accuracy and the potential improvement of the model can be inconsideration.

To prove the effectiveness of the optimization results, an additional

Table 6
Parameters of genetic algorithm.

Parameters	Value
Population size	300
Crossover fraction	0.8
Mutation fraction	0.2
Maximum generations	500
Maximum stall generation	20
Termination tolerance	10^{-6}

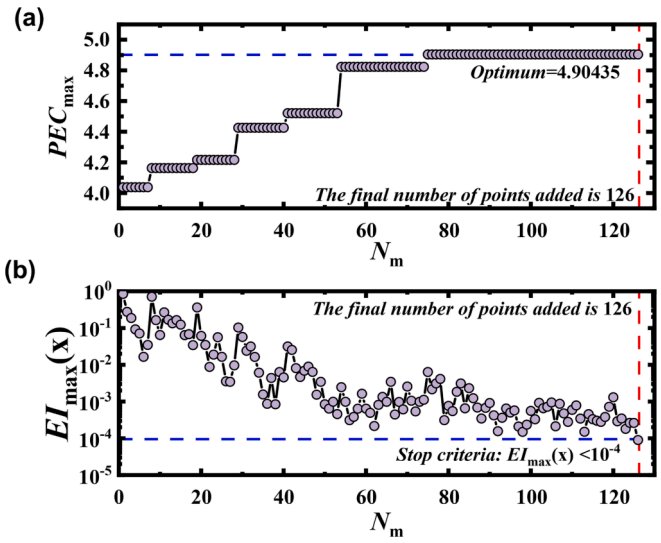

Fig. 6. Variations of $PEC_{\max}$ and $EI_{\max}$ with the number of updating model N_m (a) $PEC_{\max}$ (b) $EI_{\max}$.

set of 256 samples is obtained using a four-variable, four-level factorial design. The relationships between parameters and performance are then modeled using three traditional surrogates: RBN, SVR, and ANN models. The optimization results obtained using SML are compared with those from the traditional surrogates, as shown in Table 7. The predicted results from the three traditional surrogates all exhibit values larger than the calculated values, but within an error margin of 5%. This indicates that the actual optimization benefits are not as favorable as predicted. However, for SML, the optimal point is directly calculated as the candidate point during the model updating process, eliminating any errors. Given the high nonlinearity of the problem, the optimization results from the three models are inconsistent. Notably, the optimal *PEC* value based on SML is larger than the values obtained from the other methods, suggesting that all three methods have converged to local optimal solutions rather than achieving the global optimal value. On the other hand, choosing the number for invoking CFD solver as an efficiency indicator, the method of SML invokes the CFD solver only 166 times and the optimization efficiency increased by 35.16% compared to the 256 points required by the three traditional surrogates.

Optimal result analysis

The final optimal result is listed as Table 8 and the arrangement is depicted in Fig. 7. The distribution of the dimples is changed considerably. Five dimples in a periodic unit are joined to form a V-shaped dimpled strip in the center of the design unit surface. *Di* is located at the forefront of the strip, and *Df* and *Dc* are located obliquely posterior to *Di*.

The flow field characteristics

The 3D streamlines near the wall before and after optimization are elaborated in Fig. 8. As shown in Fig. 8 (a), most of the streamline keeps along the mainstream direction. Part of the fluid near the wall wraps around the dimple and the flow is disturbed due to the obstruction of the convex structure resulting in the formation of the flow dead zone downstream of the dimple. As the arrangement is optimized, the streamline is shown in Fig. 8 (b). Velocities perpendicular to the mainstream are induced by dimple combination, thus making the fluid flows spirally forward. Under such a flow pattern, there is more complete contact between the wall and the fluid.

The comparison of cross-sectional streamlines at different positions in a fully developed design unit is given in Fig. 9. Four cross sections uniformly distributed in the design unit are employed. The streamlines with the optimized arrangement have a significant variation from the

Table 7
Optimization results based on different surrogates.

Surrogate	Invoking number	Optimization results					*PEC* calculated by CFD	Predicted error
		X1(mm)	X2(mm)	X3(mm)	X4(°)	PEC_{pred}		
RBN	256	19.423	12.07	18.607	29.386	4.538	4.381	3.59%
SVM	256	18.136	8.741	12.39	30	4.657	4.438	4.94%
ANN	256	19.333	12.864	19.251	28.562	4.509	4.362	3.38%
SML	166	22.501	16.283	20.375	27.043	4.904	4.904	–

Table 8
Parameters before and after optimization for arrangement of dimples.

Parameters	Original design	Optimized design
d_1	7.5 mm	22.500 mm
d_2	7.5 mm	16.283 mm
d_3	22.5 mm	20.375 mm
β	30°	27.043°

comparison. Three pairs of fully developed longitudinal vortices are formed in tubes. And as the flow progresses, new longitudinal vortices continue to develop and are sustained into the next unit, ensuring a relatively high vortex intensity throughout the entire test section. This is further supported by the velocity contours shown in Fig. 10. In the optimized design, swirl flow, spiral flow, and secondary flow predominantly occur near the dimples, resulting in their significant influence on the main flow zone and the uniformity of velocity distribution improved [33]. Furthermore, the configurations of the passive devices strongly impact the fluid flow within the pipe, leading to accelerated velocity. The velocity spreads towards the radial direction, disrupting the fully developed velocity boundary layer and inducing a rotational flow along the circumferential direction near the wall. As a result, the low-speed zone near the wall is compressed.

Fig. 11 illustrates the relative pressure distributions for the original and optimized designs in two periodic units along the flow direction, derived using the reference value of the initial cross-sectional pressure. The consistent trend of decreasing relative pressure drop in the two units indicates that the flow is fully developed. Due to the sudden convergence of the tube wall, there is a noticeable pressure drop at the upstream half of the dimples. As the flow progresses, the tube expands downstream of the dimples, resulting in an increase in pressure. The original design exhibits two fluctuations in pressure distribution within

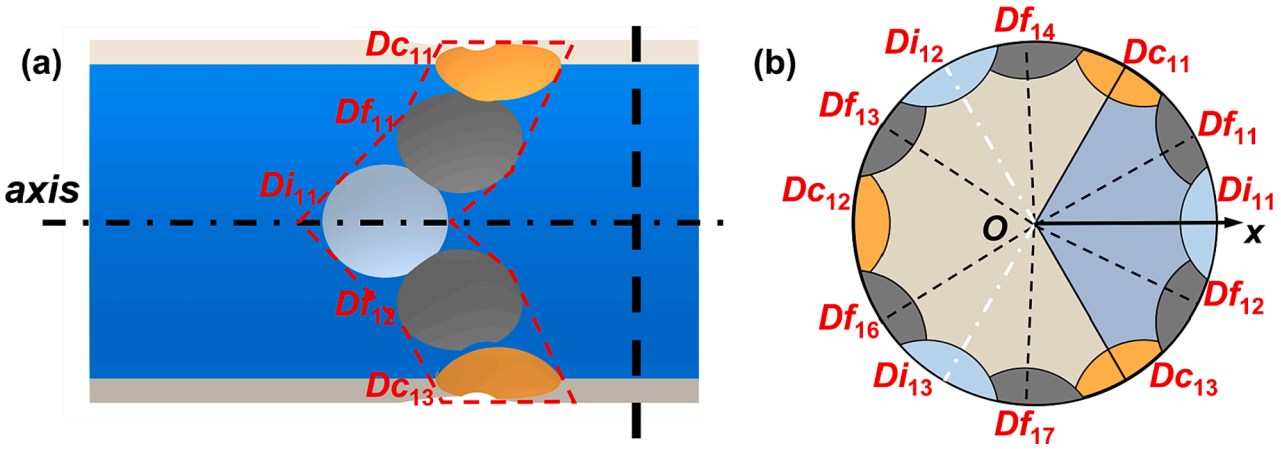

Fig. 7. Optimal design for the dimpled arrangement at $Re = 1000$ (a) front view (b) side view.

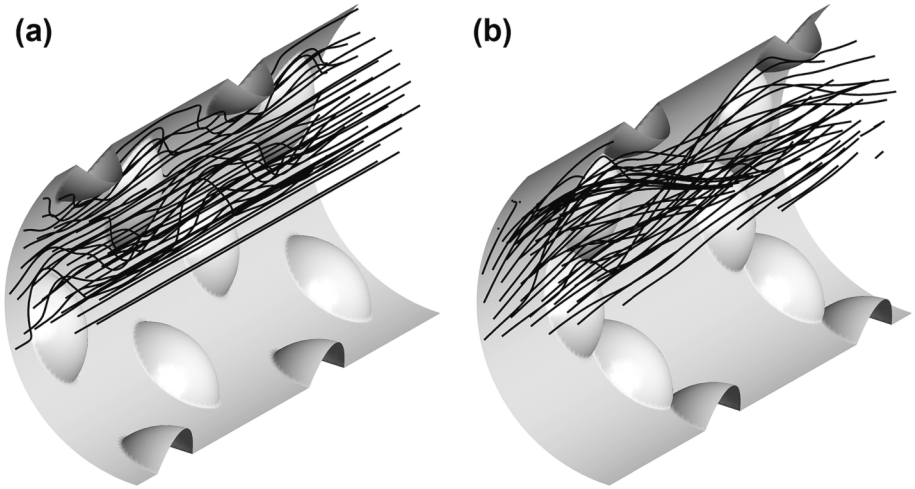

Fig. 8. 3-D streamlines near the wall for enhanced tube (a) original design (b) optimized design.

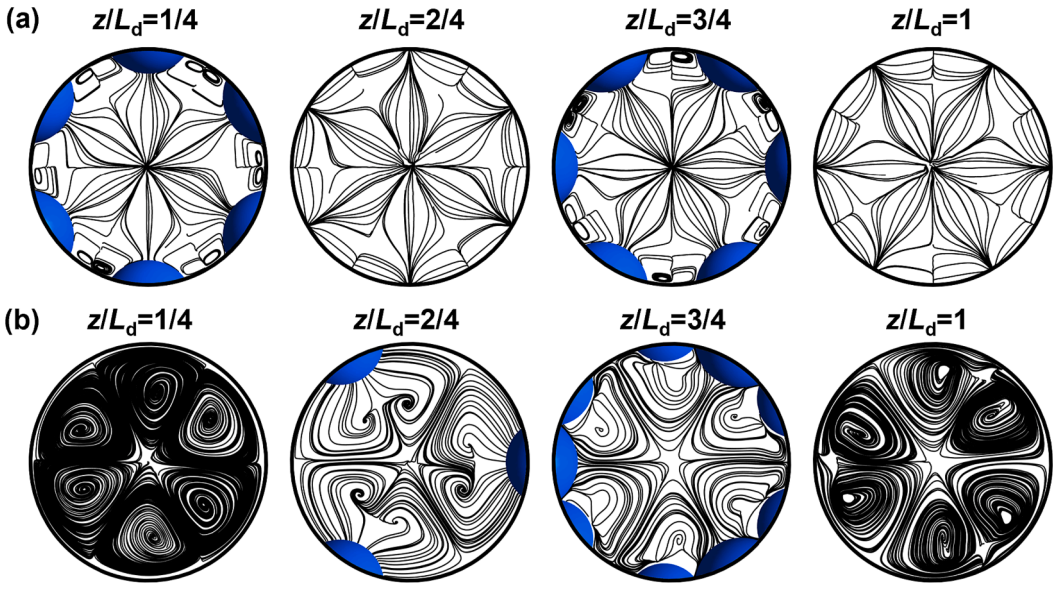

Fig. 9. Streamlines on the cross sections at $Re = 1000$ (a) original design (b) optimized design.

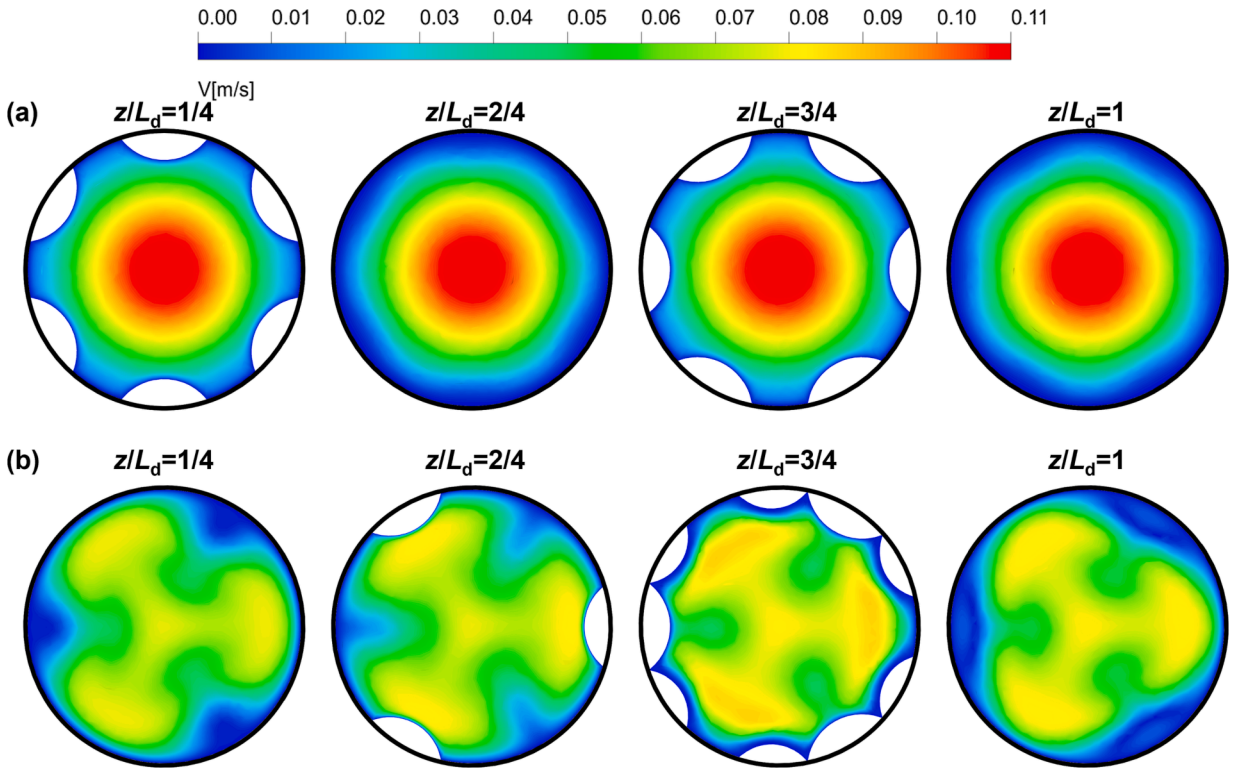

Fig. 10. Velocity contours on the cross sections at $Re = 1000$ (a) original design (b) optimized design.

a periodic unit. With the uniform distribution of the dimples, the relative pressure variations have the same magnitude for each fluctuation. In the optimized design, the pressure fluctuates only once in a periodic unit as the dimples gather and merge into a dimpled strip. The dimples are subjected to the frontal impact of the fluid, successively, resulting in a slightly higher pressure drop compared to before optimization. This higher pressure drop can be attributed to two main reasons [34]. The first one is caused by dynamic pressure dissipation of fluid flow produced by both combined impacts of the flow obstruction with the mixing and swirling flows prompted through the improved devices. The second one is due to improve the fluid flow contact region.

The heat transfer characteristics

The temperature distribution of the fluid inside the tube before and after optimization is shown in Fig. 12. The fluid is fully developed in the smooth tube, and the temperature boundary layers merge before flowing into the test section, forming a distribution with high fluid temperature near the wall and low fluid temperature in the core domain. After entering the test section, the boundary layer in the original design is not destroyed due to the limited disturbance of the dimple structure, and the high and low temperature fluid separation is still obvious, which limited the heat transfer from the wall to the fluid. In the optimized design, the intensity of flow perturbation is significantly increased, promoting the

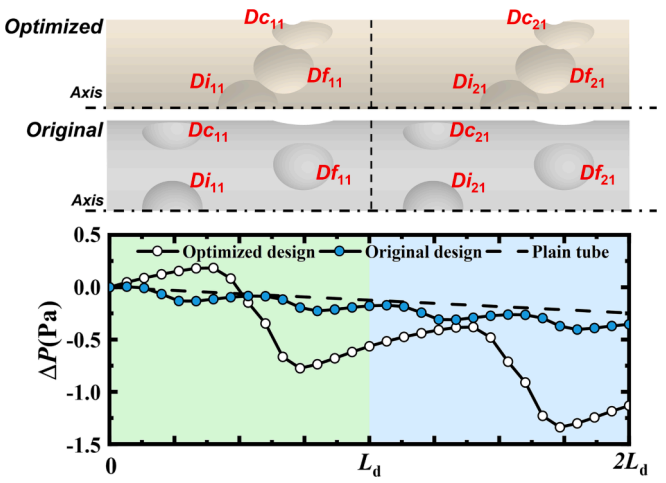

Fig. 11. Relative pressure distributions for the original and optimized design.

mixing of high-temperature fluid at the wall with low-temperature fluid in the core domain. This results in a more uniform temperature distribution and enhanced heat transfer rate [35].

The rapid mixing of high and low temperature fluids and the development of multiple longitudinal vortices at the beginning of the test section leads to unstable heat transfer. After flowing through several periodic sections, the flow pattern gradually develops and forms a definite structure due to the deflecting action, thus allowing the heat transfer intensity to remain stable in the subsequent unit. The fully developed unit are extracted and the temperature distributions of the cross sections at four different locations are given separately, as shown in Fig. 13. By comparison, it is easy to see that after the arrangement of dimples is optimized, due to the tangential velocity perpendicular to the mainstream direction is generated, it promotes the mixing of the high temperature fluid near the wall and the cold air in the core region. On the one hand, it forms a more uniform temperature distribution in the cross-section and reducing the irreversible losses in the heat transfer process. On the other hand, the longitudinal swirl flow continuously scours the tube wall, compressing the thickness of the temperature boundary layer, making a larger temperature gradient within a smaller distance of the wall, thus enhancing the convective heat transfer between the wall and the fluid [36].

Fig. 14 gives the convective heat transfer coefficient distributions for the original and optimized design in two periodic units along the flow direction. The convective heat transfer coefficient varies periodically indicating that heat transfer has been fully developed. For the original design, the maximum heat transfer coefficient is located at the upstream half of the dimples due to the fluid scours the wall indirectly and starts to separate from the wall here. And the uniform distribution makes the increased thermal performance is almost same at each dimple. After the arrangement is optimized, a secondary enhancement of the thermal performance appears at the upstream half of *Di* and *Df*. The convective heat transfer coefficient is significantly higher than the original design throughout the unit, which is the result of the combined effect of mixing of high and low temperature fluids, the compression of the temperature boundary layer and the extension of the effective fluid flow.

Field synergy analysis

To better comprehend the mechanism of heat transfer improvement, a related study was conducted from the perspective of synergy of the flow and temperature fields by Guo et al. [37], and the field synergy principle is proposed on this basis. The principle states that, convective

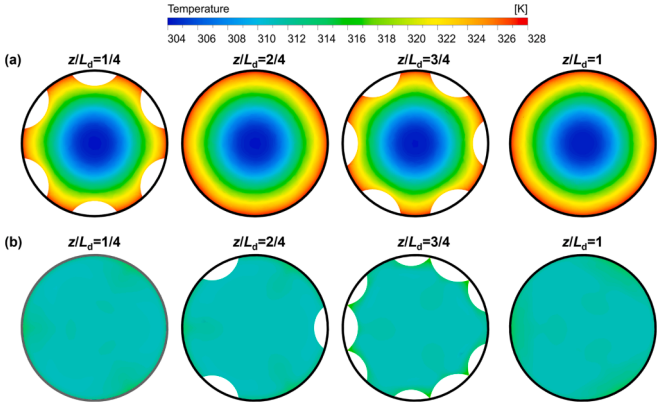

Fig. 13. Temperature contours on the cross sections at $Re = 1000$ (a) original design (b) optimized design.

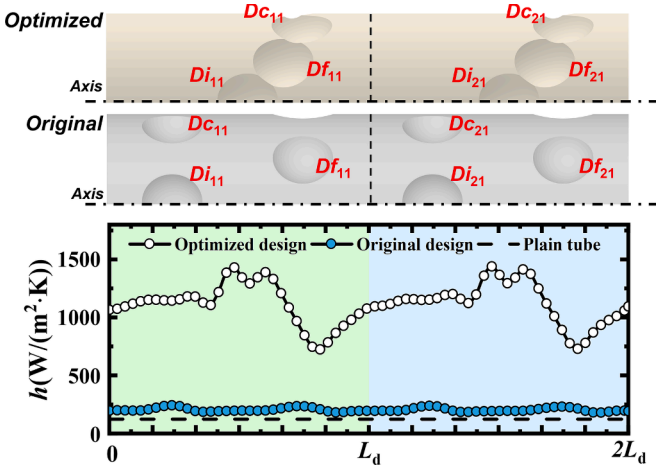

Fig. 14. Convective heat transfer coefficient distributions for the original and optimized design.

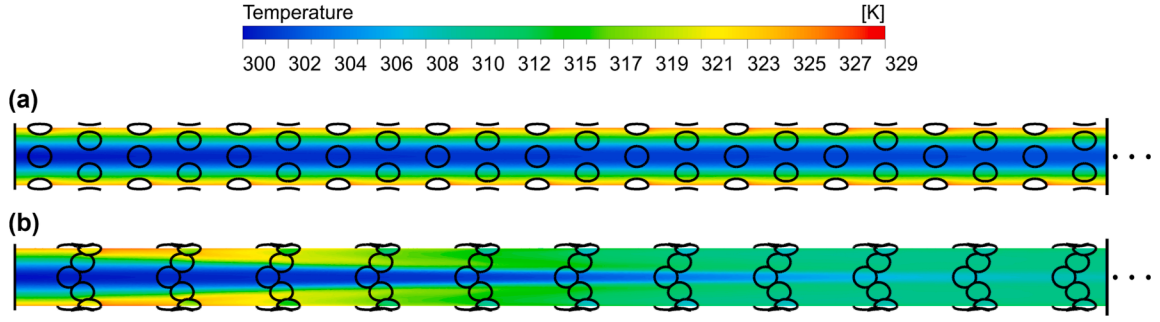

Fig. 12. Fluid temperature contours at $Re = 1000$ (a) original design (b) optimized design.

heat transfer efficiency depends not only on the velocity and heat flow distributions themselves, but also on the synergy angle between them. In general, the better heat transfer is demonstrated by the smaller angle of synergy between the velocity vector and the temperature gradient vector [38], which can be calculated as follows:

$$\alpha = \arccos\left(\frac{|\vec{U}\cdot\nabla T|}{|\vec{U}||\nabla T|}\right) \tag{18}$$

The distribution of the synergy angle at cross sections is given in Fig. 15. It is easy to see that the synergy angle distribution is affected after the installation of dimples inner the tube. For the original design, the reduced synergy angle is mainly reflected at the center of the tube. This is because the sudden contraction and expansion of the flow channel as the fluid flows through the dimples. For the optimized design, the flow is diverted strongly due to the V-shaped arrangement of the dimples, and the separated flows converge not only at the core of the tube, but also the intersections of multiple longitudinal vortices, resulting in a more significant reduction in the synergy angle. The converging wall makes the flow more intense and the partial velocity perpendicular to the mainstream is greater, which leads to a more intense rotational flow of the fluid in the rear of the dimples. The area of the reduced synergy angle is extended and the minimum value is lower than the original design, which makes the average synergy angle reduced, confirming that a superior heat transfer performance with optimized design.

Performance evaluation

Here, for a comprehensive evaluation, the average *Nu* number, flow resistance factor, and *PEC* of the optimized structure under different *Re* (600 ~ 1200) are collected and compared with the unoptimized structure and plain tube.

The variation of thermal performance with the increasing *Re* is given in Fig. 16 (a). The thermal performance of the three configurations all increases with the increasing *Re*. Due to the complete development of the temperature boundary layer in the plain tube, the boundary layer merging leads to the temperature distribution in the tube independent of the flow velocity, so the heat transfer performance of the plain tube almost keeps unvaried with the Reynolds number. The heat transfer performance of the dimpled tube before optimization increases slightly with the increase of *Re* number, and its value is slightly higher than that of the smooth tube, which indicates that the addition of dimple structure at the wall surface contributes to the enhancement of heat transfer. However, the enhancement of heat transfer performance under this structure is limited because it is only produced by the increase of heat transfer area and the disturbance caused by the dimples. In contrast, due to the transformation of the flow pattern, there is a considerable improvement as the arrangement is optimized. With the *Re* increases continuously, the heat transfer performance of the optimized dimpled tube also is enhanced, but the growth rate of heat transfer performance is slowed down. The *Nu* number for the optimized design increases from 24.039 to 39.956 in the studied *Re* number range, and improves by 437.60% to 781.89% compared with the plain tube, which is 4.053 to 5.461 times of the unoptimized dimpled tube.

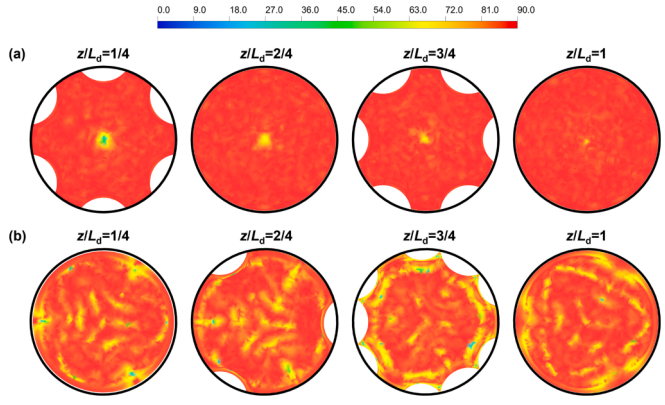

Fig. 15. Distribution of the synergy angle at cross sections (a) original design (b) optimized design.

Comparing the flow resistance factor shown in Fig. 16 (b), it can be seen that the flow resistance factors of the enhanced tubes are both larger than that of the plain tube due to the obstruction of the dimples. Combined with the relative pressure distribution in the mainstream direction, the optimized dimpled tube exhibits greater flow resistance due to the flow is deflected and a longer effective flow distance requires an increased pump power to maintain the flow. Due to the smooth surface of the spherical dimple and the presence of partial adverse pressure behind the dimples, the increase in pump power loss in the optimized design is not significant compared to that before optimization. Compared to the plain tube, the flow resistance factor increased by a maximum of 426.43% at $Re = 1200$, while increased by only 210.15% at $Re = 600$. Compared to the uniform arrangement of the dimples, The flow resistance factor inside the tube increased by 126.69% to 250.63% as the arrangement optimized.

Fig. 16 (c) gives the variation of the *PEC* with the increased *Re*. The *PEC* value of the smooth tube is constant equal to 1, and the values of two enhanced tubes are both greater than 1, which indicates that the enhanced tube has better heat transfer thermal than smooth tube with the same pump power loss. As the *Re* number increases, the values of both structures increase, indicating that the more intense the flow is, the better the overall performance for the enhanced tube. Compared to the enhanced heat transfer performance, the increase in flow resistance of the optimized dimpled tube is not significant enough, is unable to offset the gains from the improved heat transfer performance, so the design has a larger *PEC* value with a maximum of 5.069 at $Re = 1200$, while the minimum value still remains over 3.683 at $Re = 600$.

This research compares the overall thermal performance to earlier investigations. The cases involved in curved delta wing vortex generator reported by Deshmukh et al. [39], sinusoidal ribs by Du et al. [40], twisted-tape inserts reported by Wongcharee et al. [41], three-start spirally corrugated tube reported by Kareem et al. [42], wire coil inserts reported by García et al. [4], helical screw tape inserts reported by Sivashanmugam et al. [43], symmetrical wing longitudinal swirl generator reported by Wang et al. [44], bidirectional conical strip inserts reported by Liu et al. [45], discrete double-inclined ribs by Meng et al. [18]. It is seen from Fig. 17 that the flow resistance increases inconsiderable in the present study, and the dimpled tube with the arrangement optimized possesses more excellcent performance than other works.

PIV testing verification

The improvement of the heat transfer performance for the optimized dimpled tubes is closely related to the change of the flow field structure, particularly the realization of a multi-vortex longitudinal swirl flow pattern inside the tube. This flow pattern not only enhances the mixing of hot and cold fluids but also compresses the development of the boundary layer. In order to confirm the change of flow field structure inside the tube, this study further uses Particle Image Velocimetry (PIV) to observe the flow field structure inside the dimpled tubes before and after optimization, and to verify the simulation results.

PIV is a flow measurement technique developed with the development of laser technology and high-speed photography. It involves using a high-frequency pulsed laser and high-speed photography to capture images of tracer particles in a cross-section of the flow field and calculate the fluid's flow state within that cross-section. The test system and schematic of the stereoscopic-PIV system are shown in Fig. 18 and Fig. 19, respectively, and they mainly consist of the following components: a water supply system, laser and synchronization system, and

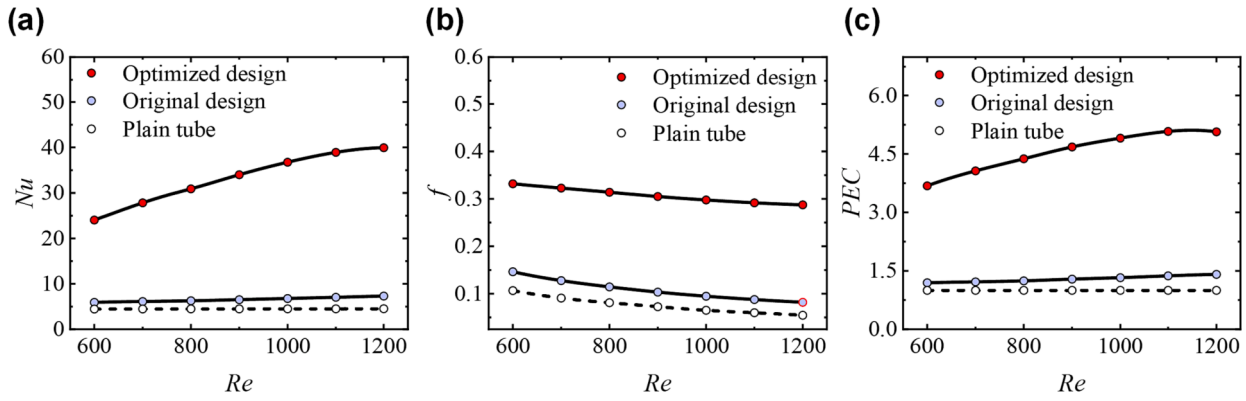

Fig. 16. The variation of performance with the increased *Re* (a) Thermal performance (b) flow resistance factor (c) *PEC*.

(b) flow resistance factor (c) *PEC*

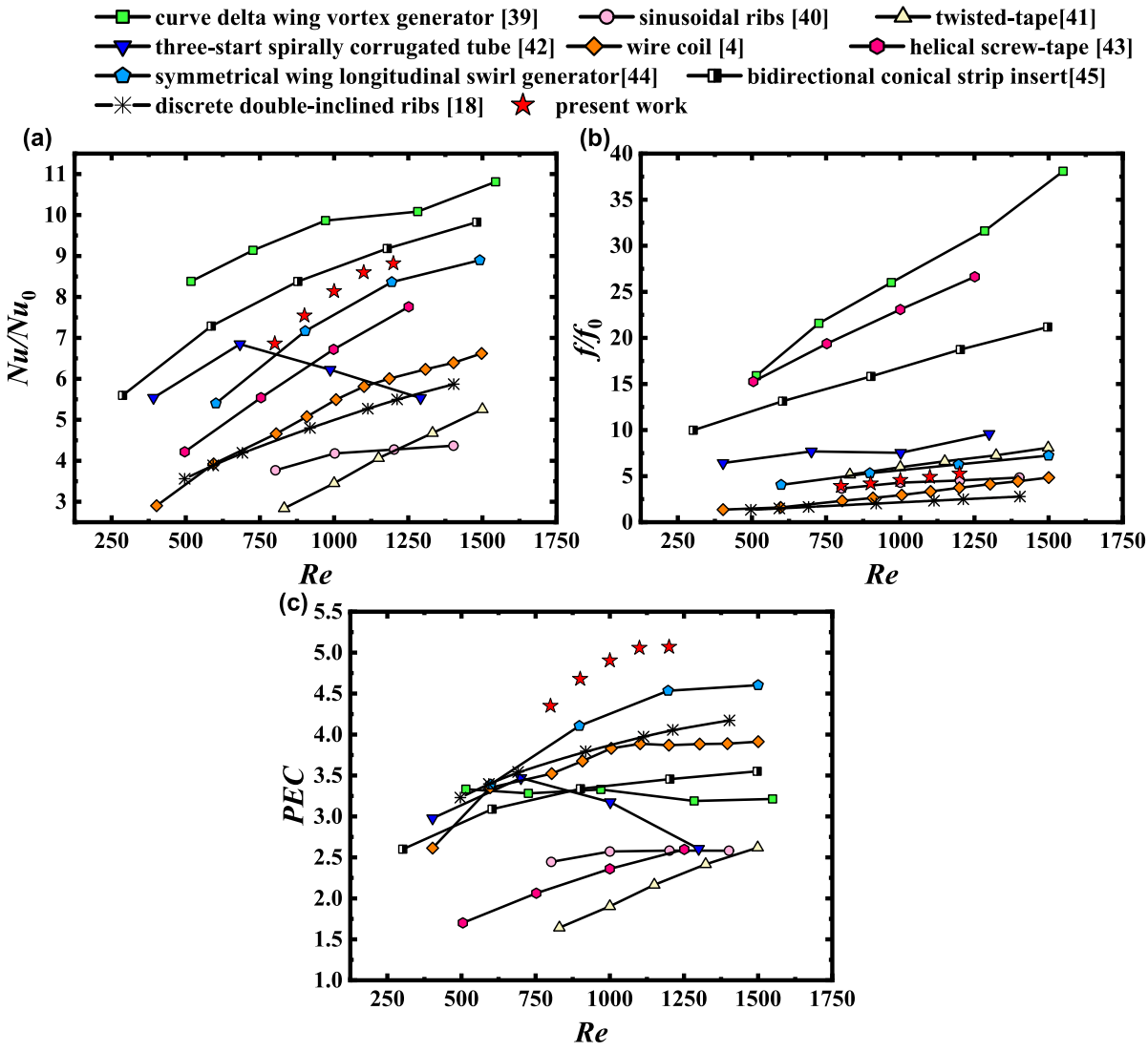

Fig. 17. Comparisons in present study with previous research (a) *Nu* number ratio (b) Flow resistance ration (c) *PEC*.

image acquisition and analysis system. The relevant experimental devices are shown in Fig. 20. The tracer particles used in the experiment is FLUOSTAR Rhodamine B particles produced by EBM corporation with the average particle size of 15 μm, a density of 1.1 g/cm^3, and a refractive index of 1.56 under laser irradiation at a wavelength of 589 nm. To ensure good light transmission and prevent image distortion due

Fig. 18. PIV test system.

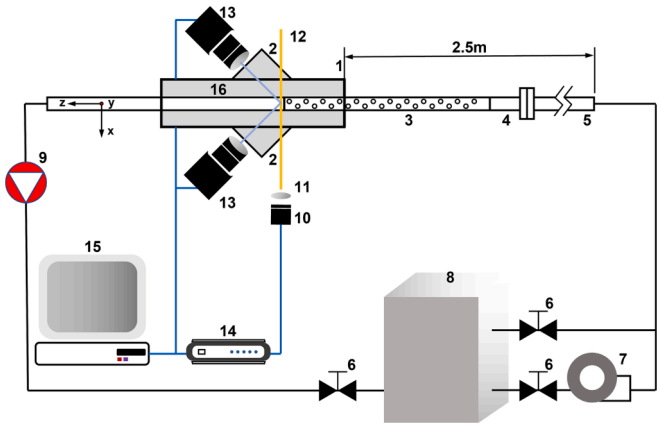

Fig. 19. Schematic of the PIV system. 1. test water box; 2. water prism; 3. test tube section; 4. entrance development section; 5. upstream tube; 6. control valves; 7. water pump; 8. water tank; 9. electromagnetic flowmeter; 10. laser; 11. lenses; 12. light sheet; 13. CCD cameras; 14. synchronizer; 15. computer; 16. observation tube section;

to refraction, the test water box, observation tube section, and water prism materials were made of transparent acrylic glass. The test tube was manufactured using curable resin and additive manufacturing technology. Before the measurement, a calibration process was carried out to determine the spatial location of the measurement section and ensure the accuracy of the PIV measurement. During the experiment, the ambient temperature was maintained at 300 K to ensure that the fluid properties were similar to those of the simulated working fluid. At the same time, the flow conditions were monitored using a flow meter to ensure stable flow with $Re = 1000$ inside the tube.

The test results and the comparison with the numerical results are shown in Fig. 21 and Fig. 22. The flow field structure in the dimpled tubes is consistent with the simulation results both before and after the optimization, which proves the validity of the numerical study in this paper. Compared with the flow field structure in the original dimpled tube, three pairs of vortexes are formed in the optimized design and the distributions are same as the numerical results, which proves that the pattern of the multi-vortex longitudinal swirl flow is constructed, and it

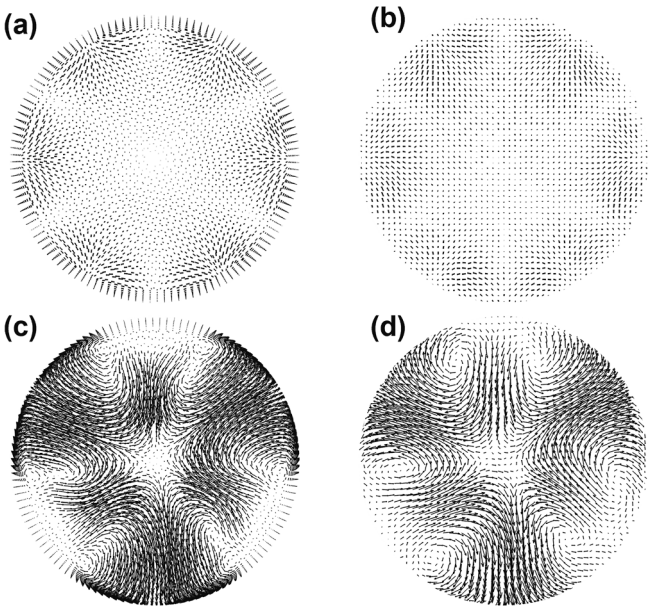

Fig. 21. Velocity vector in the observation section ($Re = 1000$) (a) numerical result for original design (b) PIV test result for original design (c) numerical result for optimized design (d) PIV test result for optimized design.

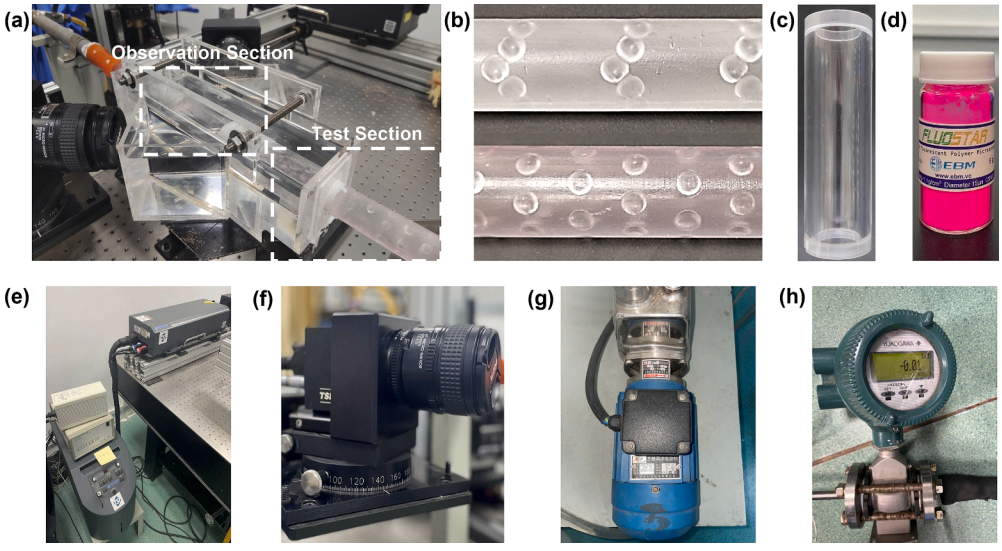

Fig. 20. Test and observation tube section and relevant experimental devices (a) test and observation tube section (b) test tube (c) observation tube (d) tracer particles (e) double pulse laser machine and synchronizer (f) CCD camera (g) water pump (h) electromagnetic flowmeter.

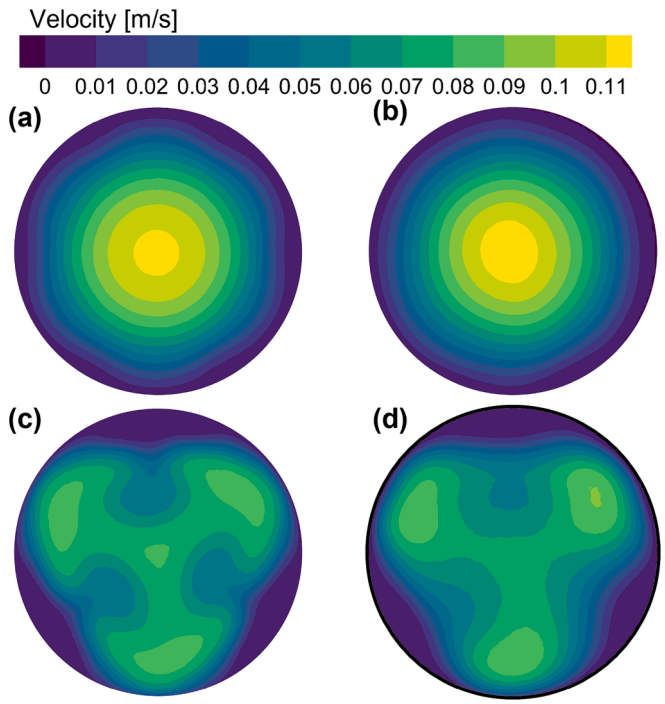

Fig. 22. Velocities comparison in the mainstream direction in the observation section (Re = 1000) (a) numerical result for original design (b) PIV test result for original design (c) numerical result for optimized design (d) PIV test result for optimized design.

is feasible to improve the flow field structure by adjusting the arrangement of the dimples for tubes.

Conclusion

The present paper mainly investigates the effect of the dimpled arrangement for the enhanced tube on the thermal–hydraulic performance. Four parameters related to the dimpled arrangement are employed as design variables and the overall performance is optimized by the method integrating with the surrogate model and machine learning techniques. The numerical work is conducted to compare the heat transfer and flow characteristics of the optimal design with the original design. The numerical results are validated by PIV test system. The conclusions can be drawn as follows:

(1) The method of surrogate based on machine learning technique is validated to exhibit high optimization efficiency and superior prediction accuracy compared to traditional surrogate models.

(2) The optimal arrangement of the dimples, where five dimples are joined to form a V-shaped dimple strip, is obtained through the proposed optimization method.

(3) The optimization of the dimple arrangement induces changes in the flow field structure within the tube, resulting in the formation of a multi-vortex longitudinal swirling flow pattern that enhances the mixing of cold and hot fluids.

(4) Under the optimal design, the heat transfer capacity is increased to 5.376–8.819 times of the plain tube with the pressure drop only increasing to 3.102–5.264 times. A *PEC* in the range of 3.683–5.069 is achieved under the involved working conditions.

(5) Particle image velocimetry experiments are conducted to obtain flow field structures that closely resemble the simulated results, thereby verifying the effectiveness of the optimization.

CRediT authorship contribution statement

Chunyu Shi: Conceptualization, Methodology, Software, Validation, Formal analysis, Investigation, Data curation, Visualization. **Yuhao Zhu:** Methodology, Software, Data curation. **Minjie Yu:** Methodology, Software. **Zhichun Liu:** Conceptualization, Resources, Supervision, Project administration, Funding acquisition.

Declaration of Competing Interest

The authors declare that they have no known competing financial interests or personal relationships that could have appeared to influence the work reported in this paper.

Data availability

the data has been involved in the manuscript

Acknowledgment

This work is Supported by the National Natural Science Foundation of China (No. 52076088), the National Key Research and Development Program of China (No. 2022YFB4003801) and the Core Technology Research Project of Shunde District, Foshan City, China (No. 2130218002932).

References

[1] W. Eng Ewe, A. Fudholi, K. Sopian, E. Solomin, M. Hossein Yazdi, N. Asim, N. Fatima, G. Pikra, H. Sudibyo, W. Fatriasari, A. Heru Kuncoro, C. Supriyadi Ali Nandar, H. Abimanyu, Jet impingement cooling applications in solar energy technologies: Systematic literature review, Thermal Science and Engineering Progress 34 (2022) 101445.

[2] S. Ahmad Sowi, S. Abdullah, K. Sopian, The effect of linearly increasing/decreasing pitch ratio twisted tape with various progression rate and nanofluid towards the system performance, Thermal Science and Engineering Progress 25 (2021), 100979, https://doi.org/10.1016/j.tsep.2021.100979.

[3] R.K. Ajeel, W.S.I.W. Salim, K. Hasnan, Numerical investigations of heat transfer enhancement in a house shaped-corrugated channel: Combination of nanofluid and geometrical parameters, Thermal Science and Engineering Progress 17 (2020), 100376, https://doi.org/10.1016/j.tsep.2019.100376.

[4] A. García, J.P. Solano, P.G. Vicente, A. Viedma, The influence of artificial roughness shape on heat transfer enhancement: Corrugated tubes, dimpled tubes and wire coils, Appl. Therm. Eng. 35 (2012) 196–201, https://doi.org/10.1016/j.applthermaleng.2011.10.030.

[5] P.G. Vicente, A. Garcia, A. Viedma, Experimental study of mixed convection and pressure drop in helically dimpled tubes for laminar and transition flow, Int. J. Heat Mass Transf. 45 (2002) 5091–5105, https://doi.org/10.1016/S0017-9310(02)00215-6.

[6] P. Kumar, A. Kumar, S. Chamoli, M. Kumar, Experimental investigation of heat transfer enhancement and fluid flow characteristics in a protruded surface heat exchanger tube, Exp. Therm Fluid Sci. 71 (2016) 42–51, https://doi.org/10.1016/j.expthermflusci.2015.10.014.

[7] R.P. Saini, J. Verma, Heat transfer and friction factor correlations for a duct having dimple-shape artificial roughness for solar air heaters, Heat transfer and friction factor correlations for a duct having dimple-shape artificial roughness for solar air heaters 33 (8) (2008) 1277–1287.

[8] M. Li, T.S. Khan, E. Al Hajri, Z.H. Ayub, Geometric optimization for thermal-hydraulic performance of dimpled enhanced tubes for single phase flow, Appl. Therm. Eng. 103 (2016) 639–650, https://doi.org/10.1016/j.applthermaleng.2016.04.141.

[9] R. Sabir, M.M. Khan, N.A. Sheikh, I.U. Ahad, D. Brabazon, Assessment of thermo-hydraulic performance of inward dimpled tubes with variation in angular orientations, Appl. Therm. Eng. 170 (2020), 115040, https://doi.org/10.1016/j.applthermaleng.2020.115040.

[10] S. Xie, Z. Liang, J. Zhang, L. Zhang, Y. Wang, H. Ding, Numerical investigation on flow and heat transfer in dimpled tube with teardrop dimples, Int. J. Heat Mass Transf. 131 (2019) 713–723, https://doi.org/10.1016/j.ijheatmasstransfer.2018.11.112.

[11] F. Zhang, X. Wang, J. Li, Flow and heat transfer characteristics in rectangular channels using combination of convex-dimples with grooves, Appl. Therm. Eng. 113 (2017) 926–936, https://doi.org/10.1016/j.applthermaleng.2016.11.047.

[12] S. Xie, Z. Liang, L. Zhang, Y. Wang, H. Ding, J. Zhang, Numerical investigation on heat transfer performance and flow characteristics in enhanced tube with dimples and protrusions, Int. J. Heat Mass Transf. 122 (2018) 602–613, https://doi.org/10.1016/j.ijheatmasstransfer.2018.01.106.

[13] J. Liu, S. Chen, M. Gan, Q. Chen, Heat transfer and flow resistance characteristics inside an innovative vortex enhanced tube, Appl. Therm. Eng. 144 (2018) 702–710, https://doi.org/10.1016/j.applthermaleng.2018.04.082.

[14] G.S. Waghmare, R.R. Arakerimath, Prediction and optimization of multipoint dimple sheet forming of structural steel using Taguchi method, Mater. Today:. Proc. 45 (2021) 5102–5107, https://doi.org/10.1016/j.matpr.2020.12.1243.
[15] T. Dagdevir, O. Keklikcioglu, V. Ozceyhan, Heat transfer performance and flow characteristic in enhanced tube with the trapezoidal dimples, Int. Commun. Heat Mass Transfer 108 (2019), 104299, https://doi.org/10.1016/j.icheatmasstransfer.2019.104299.
[16] L. Zhang, W. Xiong, J. Zheng, Z. Liang, S. Xie, Numerical analysis of heat transfer enhancement and flow characteristics inside cross-combined ellipsoidal dimple tubes, Case Studies in Thermal Engineering 25 (2021), 100937, https://doi.org/10.1016/j.csite.2021.100937.
[17] F. Ahmad, S. Mahmud, M.M. Ehsan, M. Salehin, Thermo-hydrodynamic performance evaluation of double-dimpled corrugated tube using single and hybrid nanofluids, International Journal of Thermofluids 17 (2023), 100283, https://doi.org/10.1016/j.ijft.2023.100283.
[18] J. Meng, X. Liang, Z. Li, Field synergy optimization and enhanced heat transfer by multi-longitudinal vortexes flow in tube, Int. J. Heat Mass Transf. 48 (2005) 3331–3337, https://doi.org/10.1016/j.ijheatmasstransfer.2005.02.035.
[19] K. Guo, B. Liu, X. Li, H. Liu, C. Liu, Flow pattern construction-based tubular heat transfer intensification using calculus of variations, Chem. Eng. Sci. 152 (2016) 568–578, https://doi.org/10.1016/j.ces.2016.06.046.
[20] W. Liu, P. Liu, J. Wang, N. Zheng, Z. Liu, Exergy destruction minimization: A principle to convective heat transfer enhancement, Int. J. Heat Mass Transf. 122 (2018) 11–21, https://doi.org/10.1016/j.ijheatmasstransfer.2018.01.048.
[21] J. Lv, Z. Liu, W. Liu, Active design for the tube insert of center-connected deflectors based on the principle of exergy destruction minimization, Int. J. Heat Mass Transf. 150 (2020), 119260, https://doi.org/10.1016/j.ijheatmasstransfer.2019.119260.
[22] X. Wang, N. Zheng, Z. Liu, W. Liu, Numerical analysis and optimization study on shell-side performances of a shell and tube heat exchanger with staggered baffles, International Journal of Heat and Mass Transfer 124 (2018) 247–259, https://doi.org/10.1016/j.ijheatmasstransfer.2018.03.081.
[23] J. Park, I.W. Sandberg, Universal Approximation Using Radial-Basis-Function Networks, Neural Comput. 3 (1991) 246–257, https://doi.org/10.1162/neco.1991.3.2.246.
[24] S. Ulaganathan, I. Couckuyt, D. Deschrijver, E. Laermans, T. Dhaene, A Matlab toolbox for Kriging metamodelling, Procedia - Procedia Computer Science 51 (2015) 2708–2713.
[25] C. Chang, C. Lin, LIBSVM: A Library for support vector machines, ACM Trans. Intell. Syst. Technol. 2 (2011) 1–27, https://doi.org/10.1145/1961189.1961199.
[26] A. Samad, K.-D. Lee, K.-Y. Kim, Kim ÆKLÆK, Multi-objective optimization of a dimpled channel for heat transfer augmentation 45 (2) (2008) 207–217.
[27] A. Samad, K.D. Lee, K.Y. Kim, Shape optimization of a dimpled channel to enhance heat transfer using a weighted-average surrogate model, Heat Transfer Eng. 31 (2010) 1114–1124, https://doi.org/10.1080/01457631003640453.
[28] H.M. Kim, M.A. Moon, K.Y. Kim, Multi-objective optimization of a cooling channel with staggered elliptic dimples, Energy 36 (2011) 3419–3428, https://doi.org/10.1016/j.energy.2011.03.043.
[29] X. Lei, J. Shuang, P. Yang, Y. Liu, International Journal of Heat and Mass Transfer Parametric study and optimization of dimpled tubes based on Response Surface Methodology and desirability approach, Int. J. Heat Mass Transf. 142 (2019), 118453, https://doi.org/10.1016/j.ijheatmasstransfer.2019.118453.
[30] P. Liu, Z. Dong, H. Xiao, Z. Liu, W. Liu, Thermal-hydraulic performance analysis of a novel parabolic trough receiver with double tube for solar cascade heat collection, Energy 219 (2021), 119566, https://doi.org/10.1016/j.energy.2020.119566.
[31] C. Shi, M. Wang, J. Yang, W. Liu, Z. Liu, Performance analysis and multi-objective optimization for tubes partially filled with gradient porous media, Appl. Therm. Eng. 188 (2021), 116530, https://doi.org/10.1016/j.applthermaleng.2020.116530.
[32] Y. Ge, Z. Liu, W. Liu, Multi-objective genetic optimization of the heat transfer for tube inserted with porous media, Int. J. Heat Mass Transf. 101 (2016) 981–987, https://doi.org/10.1016/j.ijheatmasstransfer.2016.05.118.
[33] A.R. Al-Obaidi, J. Alhamid, Investigation of thermo-hydraulics flow and augmentation of heat transfer in the circular pipe by combined using corrugated tube with dimples and fitted with varying tape insert configurations, Int. J. Heat Technol. 39 (2021) 365–374. https://doi.org/10.18280/ijht.390205.
[34] A.R. Al-Obaidi, J. Alhamid, Investigation of flow pattern, thermohydraulic performance and heat transfer improvement in 3D corrugated circular pipe under varying structure configuration parameters with development different correlations, International Communications in Heat and Mass Transfer 126 (2021), 105394, https://doi.org/10.1016/j.icheatmasstransfer.2021.105394.
[35] J. Alhamid, A.R. Al-Obaidi, H. Towsyfyan, A numerical study to investigate the effect of turbulators on thermal flow and heat performance of a 3D pipe, Heat Transfer 51 (2022) 2458–2475, https://doi.org/10.1002/htj.22407.
[36] J. Alhamid, R.A. Al-Obaidi, Flow Pattern Investigation and Thermohydraulic Performance Enhancement in Three-Dimensional Circular Pipe under Varying Corrugation Configurations, Journal of Physics: Conference Series 1845 (1) (2021) 012061.
[37] Z. Guo, D. Li, B. Wang, A novel concept for convective heat transfer enhancement, Int. J. Heat Mass Transf. 41 (1998) 2221–2225, https://doi.org/10.1016/S0017-9310(97)00272-X.
[38] Y. Liu, Y. Dong, L. Xie, C. Zhang, C. Xu, Heat transfer enhancement of supercritical CO 2 in solar tower receiver by the field synergy principle, Appl. Therm. Eng. 212 (2022), 118479, https://doi.org/10.1016/j.applthermaleng.2022.118479.
[39] P.W. Deshmukh, S.V. Prabhu, R.P. Vedula, Heat transfer enhancement for laminar flow in tubes using curved delta wing vortex generator inserts, Appl. Therm. Eng. 106 (2016) 1415–1426, https://doi.org/10.1016/j.applthermaleng.2016.06.120.
[40] J. Du, Y. Hong, S.M. Huang, W.B. Ye, S. Wang, Laminar thermal and fluid flow characteristics in tubes with sinusoidal ribs, Int. J. Heat Mass Transf. 120 (2018) 635–651, https://doi.org/10.1016/j.ijheatmasstransfer.2017.12.047.
[41] K. Wongcharee, S. Eiamsa-ard, Friction and heat transfer characteristics of laminar swirl flow through the round tubes inserted with alternate clockwise and counter-clockwise twisted-tapes, Int. Commun. Heat Mass Transfer 38 (2011) 348–352, https://doi.org/10.1016/j.icheatmasstransfer.2010.12.007.
[42] Z.S. Kareem, S. Abdullah, T.M. Lazim, M.N. Mohd Jaafar, A.F. Abdul Wahid, Heat transfer enhancement in three-start spirally corrugated tube: Experimental and numerical study, Chem. Eng. Sci. 134 (2015) 746–757, https://doi.org/10.1016/j.ces.2015.06.009.
[43] P. Sivashanmugam, S. Suresh, Experimental studies on heat transfer and friction factor characteristics of laminar flow through a circular tube fitted with helical screw-tape inserts, Appl. Therm. Eng. 26 (2006) 1990–1997, https://doi.org/10.1016/j.applthermaleng.2006.01.008.
[44] Y. Wang, P. Liu, H. Xiao, Z. Liu, W. Liu, Design and optimization on symmetrical wing longitudinal swirl generators in circular tube for laminar flow, Int. J. Heat Mass Transf. 193 (2022), 122961, https://doi.org/10.1016/j.ijheatmasstransfer.2022.122961.
[45] P. Liu, N. Zheng, F. Shan, Z. Liu, W. Liu, Heat transfer enhancement for laminar flow in a tube using bidirectional conical strip inserts, Int. J. Heat Mass Transf. 127 (2018) 1064–1076, https://doi.org/10.1016/j.ijheatmasstransfer.2018.07.128.